



**Research article**

## **Energy absorption and multi-objective optimization of TPMS filled cylinder shell structures**

**Laiyu Liang<sup>1</sup>, Huaiming Zhu<sup>2</sup>, Dong Wei<sup>3</sup>, Yaozhong Wu<sup>2,\*</sup> and Weijia Li<sup>4</sup>**

<sup>1</sup> Wuhan Second Ship Design and Research Institute, Wuhan 430205, China

<sup>2</sup> School of Automobile and Traffic Engineering, Wuhan University of Science and Technology, Wuhan 430081, China

<sup>3</sup> Alphapac Instrument (Hubei) Co., Ltd, Yichang 443000, China

<sup>4</sup> School of Naval Architecture & Ocean Engineering, Huazhong University of Science and Technology, Wuhan, Hubei 430074, China

**\* Correspondence:** Email: [wuyzh157@163.com](mailto:wuyzh157@163.com), [wuyaohong@wust.edu.cn](mailto:wuyaohong@wust.edu.cn); Tel: +8613377874962.

**Abstract:** Cylinder shell (CS) structures are widely applied in marine industry applications with the characteristics of high loading ability and high energy absorption performance. In this study, the triply periodic minimal surfaces (TPMS) lattices were filled into double cylinder shell structures to construct the cylinder shell (TPMS-CS) structures. The mechanical and energy absorption performances of these structures were investigated by simulation analysis. First, the finite element (FE) model of TPMS-CS structures was verified by experiments. Then, the crashworthiness characteristics of three different kinds of TPMS-CS, namely, primitive, diamond, and gyroid, under axial loading were studied using FE simulation. The results indicate that the diamond-based TPMS-CS structures exhibit a higher energy absorption efficiency compared to their counterparts. Next, parametric studies were carried out to investigate the influence of the design parameters (the relative density of the TPMS, and the inner and outer shell thickness) on the crashworthiness of TPMS-CS structures. Finally, to obtain the optimum design for the TPMS-CS, an optimization framework was proposed by combining the three surrogate models (KGR, PRS, RBF) and multi-objective particle swarm optimization. The optimum design of the D-TPMS-CS structures was obtained based on the proposed optimization framework. The TPMS-CS structures proposed in this study can also be applied in other engineering applications as energy absorbers.

**Keywords:** cylinder shell structures; triply periodic minimal surfaces (TPMS); energy absorption; multi-objective optimization

## 1. Introduction

Cylindrical shell structures, which have high specific stiffness and strength [1], high buckling resistance [2,3], and outstanding energy absorption performance [4,5], have been widely used as underwater vehicle hulls and ship propellers. Over the past decades, numerous research has been conducted to achieve more efficient structural configurations, such as composite sandwich cylindrical shells [6], lattice cylindrical shells (LCS) [7,8], and functionally graded designs [9,10]. Lattice structures, such as honeycomb [11–13], foam [14], and strut-based lattice [15,16], are widely used in the design of LCS. It has been shown that the LCS is more efficient in load-carrying and energy absorption than the cylindrical shell.

For example, Zhang et al. [17] built the FE and analytical models to study the crushing responses of the lattice cylindrical shells. The optimization design was also conducted to seek the minimum weight design of the LCS structures. It was found that the Kagome and triangular LCS possess higher load-carrying efficiency compared with the hexagonal counterpart. Chen et al. [18] investigated the deformation and failure mechanism of the graded LCS with triangular and hexagonal configurations under axial impact loading. Numerical and theoretical models were constructed based on the FE method and one-dimension shock theory. The results show that the crashworthiness performances of these LCSs are significantly affected by relative density and the density gradient along the crushing direction can enhance energy absorption for LCS structures. A hierarchical honeycomb cylindrical structure was proposed and investigated by experimental tests [19]. It was found that the proposed structure exhibits excellent deformation recovery and energy absorption capabilities.

Recently, researchers have found that the TPMS lattices possess superior mechanical and crashworthiness behaviors compared to the struct-based lattices [20,21]. For example, Zhang et al. [22] investigated the mechanical and energy absorption properties of the TPMS sheet structure to the body-centered cubic lattice by experimental and numerical methods. It was found that the TPMS sheet structures are significantly superior to body-centered lattices in mechanical and energy absorption properties. Qiu et al. [23] proposed a three-dimensional functionally graded TPMS structure and studied their mechanical properties using experimental and numerical techniques. It was found that a higher volume fraction and the proper adoption of gradient could improve the energy absorption capability of the proposed structures. Yin et al. [24] studied the energy absorption behaviors of the TPMS sheet structures under axial loading by experimental and numerical methods. It was found the crashworthiness performance was affected by the level constant and the shell thickness. Moreover, multi-objective optimization was conducted to achieve an optimal design for the TPMS sheet structures.

Nowadays, researchers have constructed LCS structures with TPMS lattices. For example, Wang et al. [8] constructed a Gyroid lattice-based cylindrical shell structure by a mapping method and studied their energy absorption and deformation modes using experimental tests and numerical simulations. The results show that the Gyroid lattice cylindrical shell exhibit superior mechanical and energy absorption properties compared to its counterparts. The parametric study showed that the energy absorption properties were significantly affected by the relative density, and geometric gradients. Following the proposed mapping method, Zhu et al. [7] proposed a modified mapping method to

design the Diamond lattice cylindrical shell structure and investigated their energy absorption performances by experimental and numerical methods. The experimental and simulation results show that deformation modes and crashworthiness performances were significantly affected by relative density, cell size, radial variation coefficient, and mapping angle.

The LCS structures should be used with surrounded shells to facilitate engineering applications. To the author's best knowledge, the crashworthiness and optimization design of the TPMS filled cylinder shell structures has not been reported to date.

In this study, the energy absorption performances of TPMS-CS structures under axial compression were investigated. Firstly, the TPMS-CS structures were designed based on the LCS and double cylindrical shells. Then, the FE model was built to simulate the crushing responses and verified by the results of the test. Parametric studies were carried out to study the influence of the relative density of the TPMS, outer shell thickness, and inner shell thickness on the energy absorption of TPMS-CS structures. Finally, the optimal design of TPMS-CS structures was achieved by a surrogate-based optimization method.

## 2. Materials and methods

### 2.1. Design

The proposed TPMS filled cylindrical shell (TPMS-CS) structure consists of a TPMS based lattice shell structure (LCS) and a double cylinder shell structure, as shown in Figure 1. The TPMS based LCSs are derived according to the mapping method proposed in ref [7,8]. Three TPMSs are used to construct the TPMS-LCSs, i.e., Primitive (P), Diamond (D), and Gyroid (G) surfaces, which can be described using the level-set function  $\varphi$  [20,25]:

$$\begin{aligned}\varphi_P(x, y, z) &= \cos(\omega x) + \cos(\omega y) + \cos(\omega z) \\ \varphi_D(x, y, z) &= \sin(\omega x)\sin(\omega y)\sin(\omega z) + \cos(\omega x)\cos(\omega y)\cos(\omega z) \\ &\quad + \sin(\omega x)\cos(\omega y)\cos(\omega z) + \cos(\omega x)\cos(\omega y)\sin(\omega z) \\ \varphi_G(x, y, z) &= \cos(\omega x)\sin(\omega y) + \cos(\omega y)\sin(\omega z) + \cos(\omega z)\sin(\omega x)\end{aligned}\quad (1)$$

where  $x, y, z$  are spatial coordinates,  $\omega = 2\pi/l$ , and  $l$  is the length of a unit cell. The sheet-based TPMS is derived from the equation  $\varphi^2 \leq c^2$ , the relative density (RD) is controlled by the constant  $c$  [25].

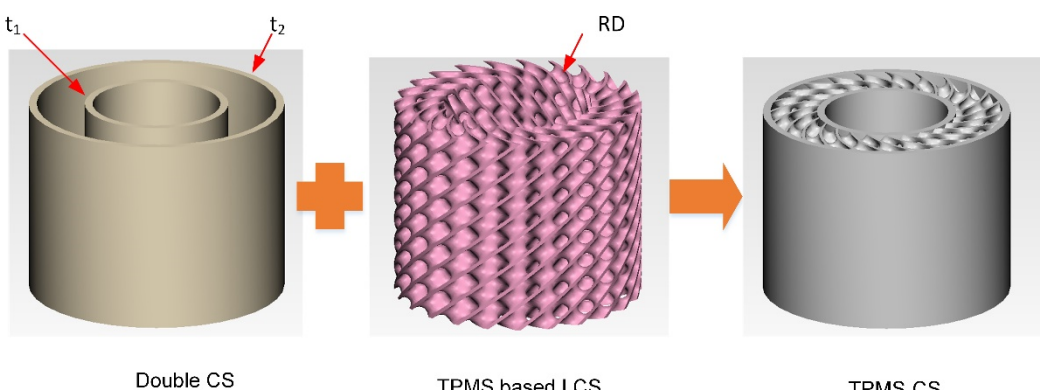


**Figure 1.** Construction of the TPMS-CS structure.

In this study, the geometric parameters of TPMS-CS structures are set as follows: height  $H = 24$  mm, outer diameter  $D_{out} = 30$  mm, inner diameter  $D_{in} = 18$  mm,  $l = 6$  mm. Three design parameters are considered in this study, namely, inner shell thickness ( $t_1$ ), outer shell thickness ( $t_2$ ), and TPMS filled relative density ( $RD$ ), as shown in Figure 1.

## 2.2. Numerical models

The FE model is built to simulate the axial crushing process of the TPMS-CS structures by commercial finite element software LS-DYNA. The established FE model of TPMS-CS is shown in Figure 2. The TPMS-CS is compressed with a rigid wall with a compressive velocity of 1 m/s and the TPMS-CS is placed on a fixed rigid wall. The rigid walls are defined as rigid bodies with the MAT-20 rigid material model. The TPMS-CS is modeled by the Belytschko-Tsay shell elements with reduced integration. The MAT-24 is used to simulate the TPMS-CS, which is made of 316L stainless steel. The base material parameters are used from the ref [7] and listed in Table 1.

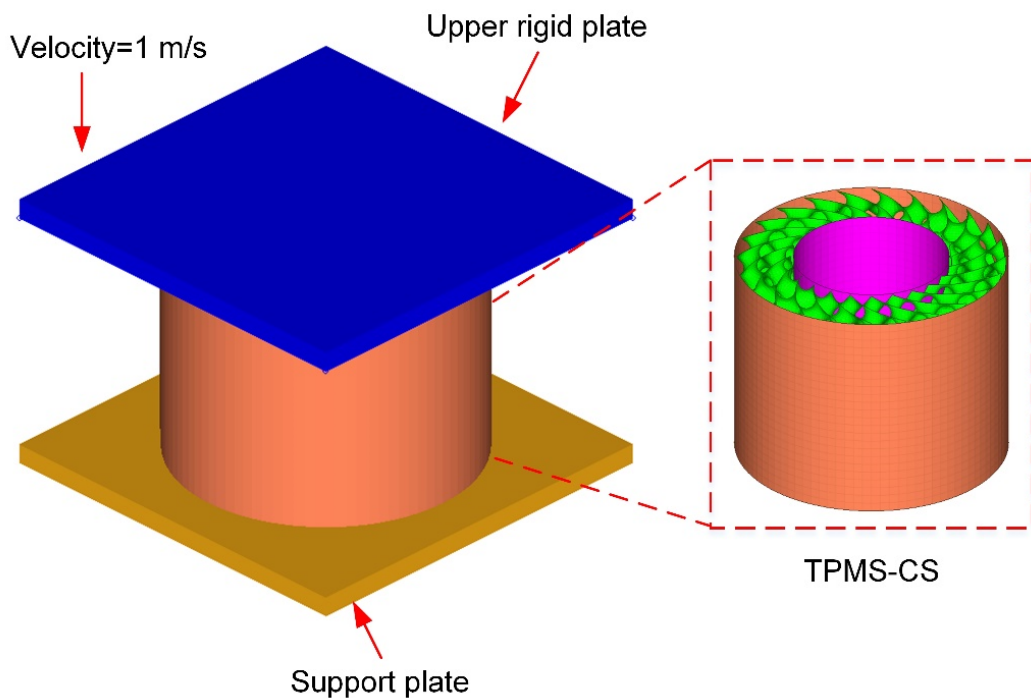


**Figure 2.** FE model of the TPMS-CS structure.

**Table 1.** Material parameters of the 316L stainless steel [7].

Parameters	Value
Density (g/cm <sup>3</sup> )	7.98
Young's modulus (GPa)	190
Yield stress (MPa)	633
Ultimate stress (MPa)	1074
Poisson's ratio	0.3

To simulate the contact between the TPMS-CS and the rigid walls, the “automatic node to surface” contact algorithm is employed in this study [26]. To account self-contact of the TPMS-CS itself during compression, the “automatic single surface” contact algorithm is adopted. For static and dynamic friction, a friction coefficient is set to 0.3 for all contact conditions [27,28]. Mesh size convergence tests are conducted to obtain the optimal mesh size, and a mesh size of 0.4 mm × 0.4 mm is adopted in this study.

### 2.3. Crashworthiness indicators

To evaluate the energy absorption properties of the TPMS-CSs, the crashworthiness indicators include Energy Absorption (EA), Specific Energy Absorption (SEA), Peak Crushing Force (PCF), and Crush Force Efficiency (CFE) are used in this study.

EA is defined as the total energy absorption of the whole energy absorber, and can be expressed as follows,

$$EA = \int_0^d F(x) dx \quad (2)$$

where  $d$  is the effective crushing distance, which is defined as the crushing distance at which energy efficiency has the maximum value [29].  $F(x)$  is the instantaneous crushing force at the crushing distance  $x$ .

SEA is used to evaluate the energy absorption efficiency of the energy absorber with different materials and weights, which is defined as the energy absorption per unit mass, and can be calculated as follows,

$$SEA = \frac{EA}{m} \quad (3)$$

where  $m$  is the mass of the structure.

The PCF is the maximum value of the crushing force during the whole crushing process. The crushing force efficiency (CFE) is the uniformity of crushing force in the crushing process, which can be calculated as follow,

$$CFE = \frac{MCF}{PCF} \times 100\% \quad (4)$$

where MCF is the average crushing force within the effective deformation distance and can be derived as follows,

$$MCF = \frac{EA}{d} \quad (5)$$

### 2.4. Validation of the numerical model

The experimental results were adopted from the reference [7] and compared with the results of the FE model which building by the above-introduced method to verify the accuracy of the FE model. In the literature, the Diamond LCS (D-LCS) was compressed with a velocity of 5 mm/min, and the deformation modes of the D-LCS and force-displacement curves of tests were recorded. The

comparisons of the deformation modes and the force-displacement curves between the reference and simulation results are shown in Figure 3. It is seen that similar deformation patterns are founded both in reference and simulation results, and the force-displacement curves are in good agreement.

Furthermore, the crashworthiness indicators of the experimental tests and simulations are listed in Table 2. The results of EA and PCF show that the error between simulation and reference results is no more than 2%, which proves the accuracy of the FE model used in this study.

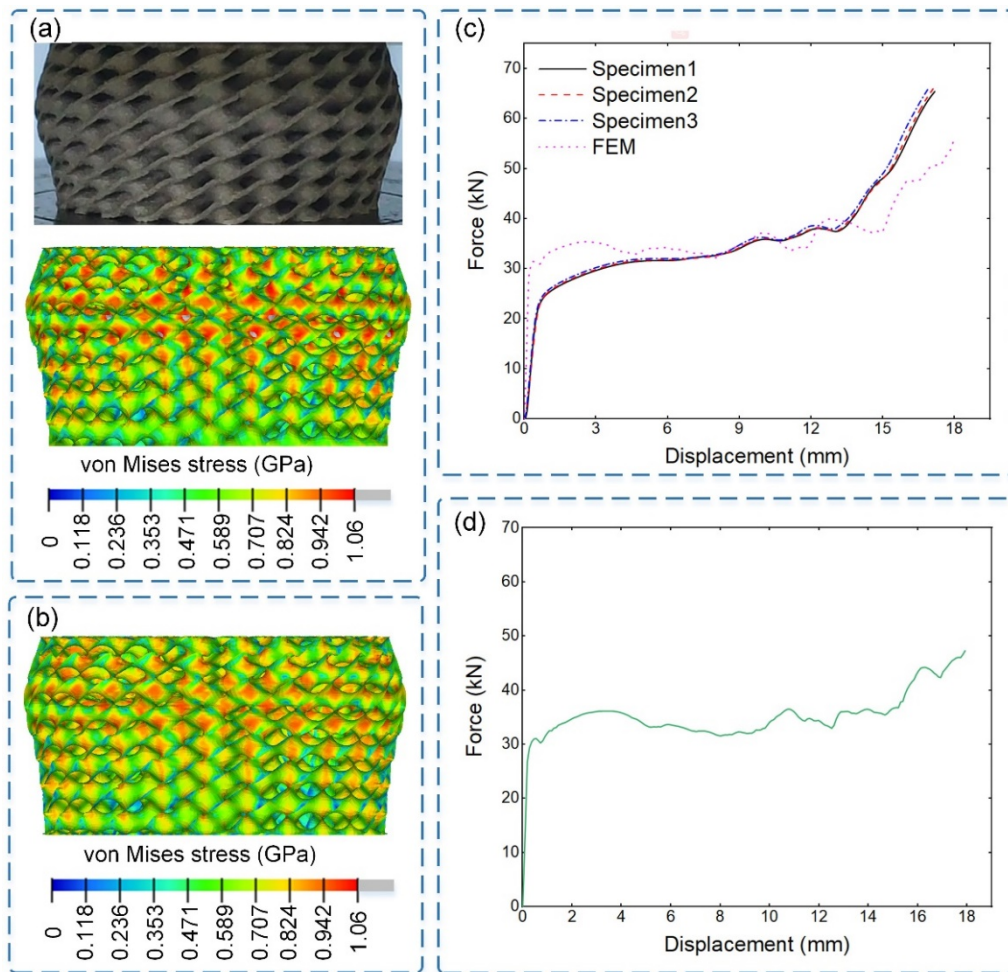


**Figure 3.** Validation of the FE models: (a) Experimental and simulation deformation patterns [7]; (b) Simulation deformation results by this paper; (c) Experimental and simulation force-displacement curves [7]; (d) Simulation force-displacement curve by this paper.

**Table 2.** Error metrics between experiment and simulation results.

Indicators	Test (average)	Reference results	This paper	Error (%)
EA (J)	633.38	669.97	672.15	0.33
PCF (kN)	65.86	66.07	65.92	-1.34

### 3. Results and discussions

#### 3.1. Energy absorption performances

Three different kinds of TPMS-CS structures (P, D, G) were investigated using FE analysis to explore their energy absorption performances. All the structures have the same structural parameters:  $t_1 = 2$  mm,  $t_2 = 2$  mm, and  $RD = 20\%$ .

Figure 4 gives the deformation modes of the three kinds of TPMS-CS structures after compression. It is shown that all the TPMS-CS structures deformed in a layer-by-layer mode, which is similar to the cylindrical shells [30].

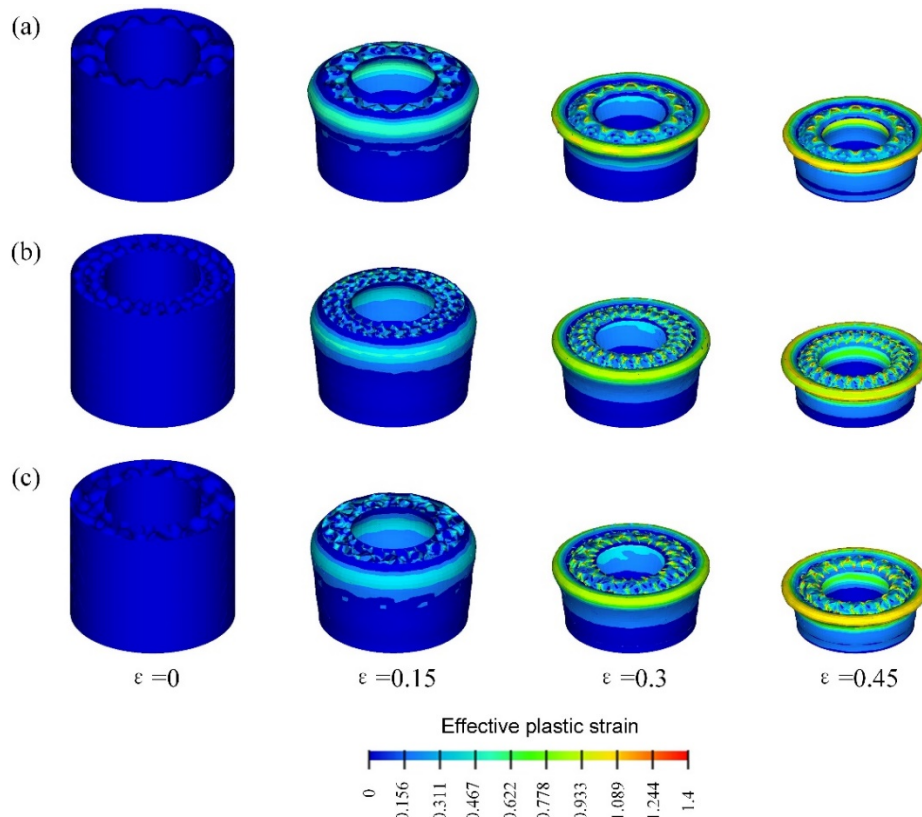


**Figure 4.** Deformation modes of the TPMS-CS at different strains: (a) P, (b) D, (c) G.

Figure 5 shows the force-displacement curves of the three TPMS-CS structures. All the TPMS-CS structures exhibit similar crushing force responses. Specifically, the plateau stress of D-TPMS-CS is higher than two other structures.

Table 3 further gives the crashworthiness indicators of the three kinds of TPMS-CS structures. The results show that the D-TPMS-CS possesses the highest EA and SEA as expected. Specifically, the SEA of D-TPMS-CS is improved by 2.7% and 3.5% compared with that of G-TPMS-CS and P-TPMS-CS, respectively. However, the PCF of D-TMPS-CS is also higher than the other two structures. For crushing force efficiency, D-TPMS-CS exhibits the highest CFE among all the TPMS-CS structures. The results indicate that the D-TPMS-CS structure exhibits better energy absorption capacity and efficiency.

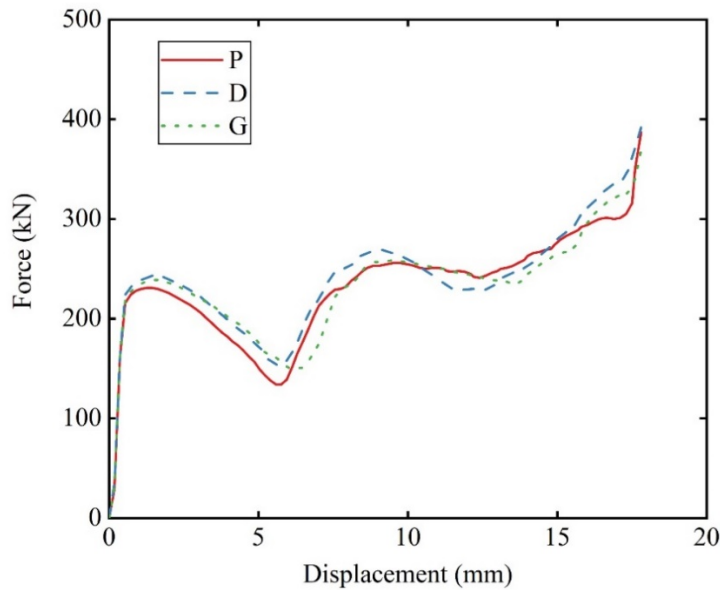


**Figure 5.** Comparison of force-displacement curves of three TPMS-CS structures.

**Table 3.** Crashworthiness indicators for the three TPMS-CS structures.

TPMS-CS	EA (J)	PCF (kN)	SEA (kJ/kg)	CFE
P	4126.79	386.62	54.98	0.59
D	4272.38	412	56.92	0.65
G	4158.38	368.61	55.40	0.63

### 3.2. Influence of design parameters

To study the effect of design parameters on the crashworthiness of the TPMS-CS structures, three design parameters, i.e., inner shell thickness ( $t_1$ ), outer shell thickness ( $t_2$ ), and the relative density of filled TPMS ( $RD$ ) were considered in this section.

#### 3.2.1. The influence of $t_1$

To investigate the effect of the inner shell thickness  $t_1$  on the crashworthiness of TPMS-CS, the FE analysis was carried out by changing the  $t_1$  from 1 mm to 3 mm. All the TPMS-CS structures have identical parameters for outer shell thickness  $t_2 = 2$  mm and  $RD = 20\%$ .

Figure 6 plots the force-displacement curves of three TPMS-CS structures with different  $t_1$ . The results show that all the curves exhibit three distinct regions: elastic deformation region, plateau stress region, and densification region. The plateau stress of all the TPMS-CS structures is improved with the increase of  $t_1$ . Interestingly, the crushing force increases rapidly at the densification region when the  $t_1$  possess a higher value.

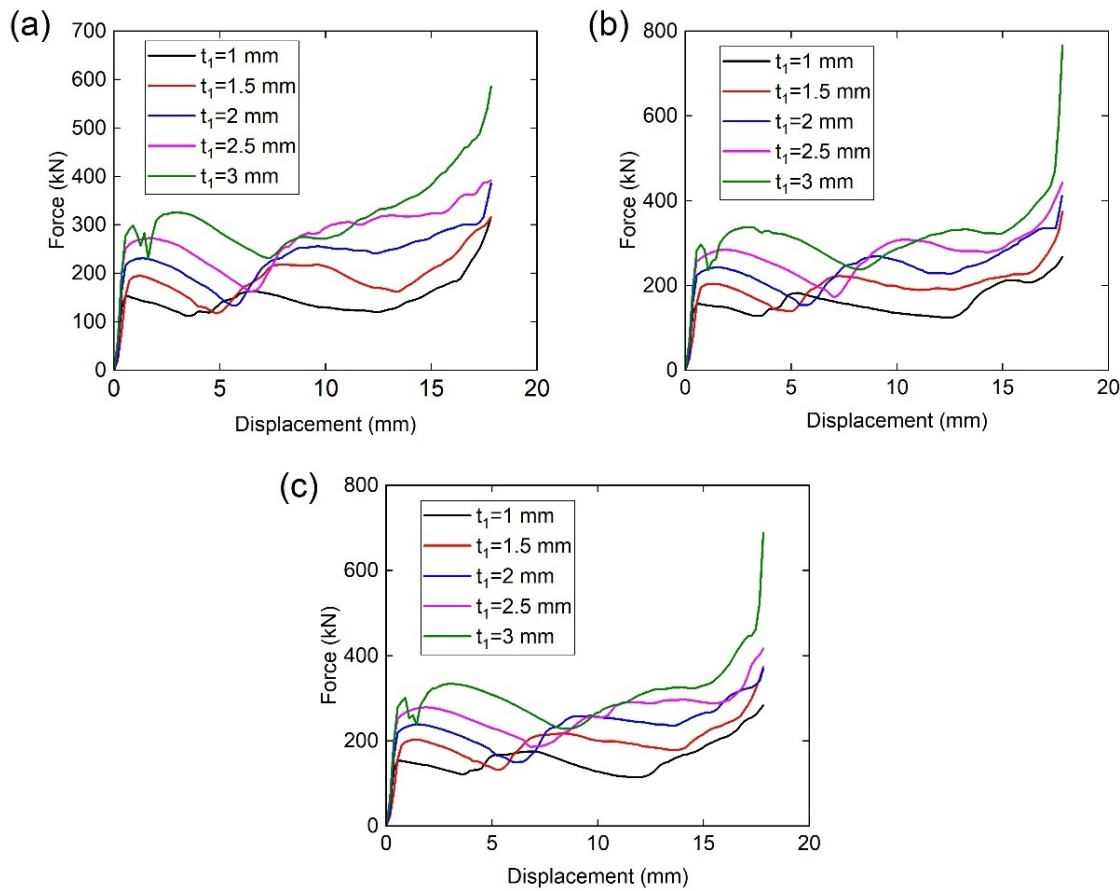


**Figure 6.** Force–displacement curves of (a) P-TPMS-CSs, (b) D-TPMS-CSs, and (c) G-TPMS-CSs for different  $t_1$ .

**Table 4.** Influence of  $t_1$  on crashworthiness indicators of TPMS-CS structures.

TPMS	$t_1$ (mm)	EA (J)	PCF (kN)	SEA (kJ/kg)	CFE
P	1	2624.98	316.75	46.34	0.46
	1.5	3367.45	316.55	51.13	0.59
	2	4126.79	386.62	54.98	0.59
	2.5	4872.01	391.79	57.81	0.69
	3	5623.44	585.47	60.16	0.53
D	1	2861.39	268	50.51	0.59
	1.5	3539.74	374.37	53.75	0.6
	2	4272.38	412	56.92	0.65
	2.5	4849.31	443.49	57.55	0.7
	3	5556.85	657.25	59.45	0.54
G	1	2795.62	283.27	49.34	0.55
	1.5	3495.27	373.79	53.07	0.52
	2	4158.38	368.61	55.40	0.63
	2.5	4676.69	417.58	55.50	0.62
	3	5441.84	688.81	58.22	0.44

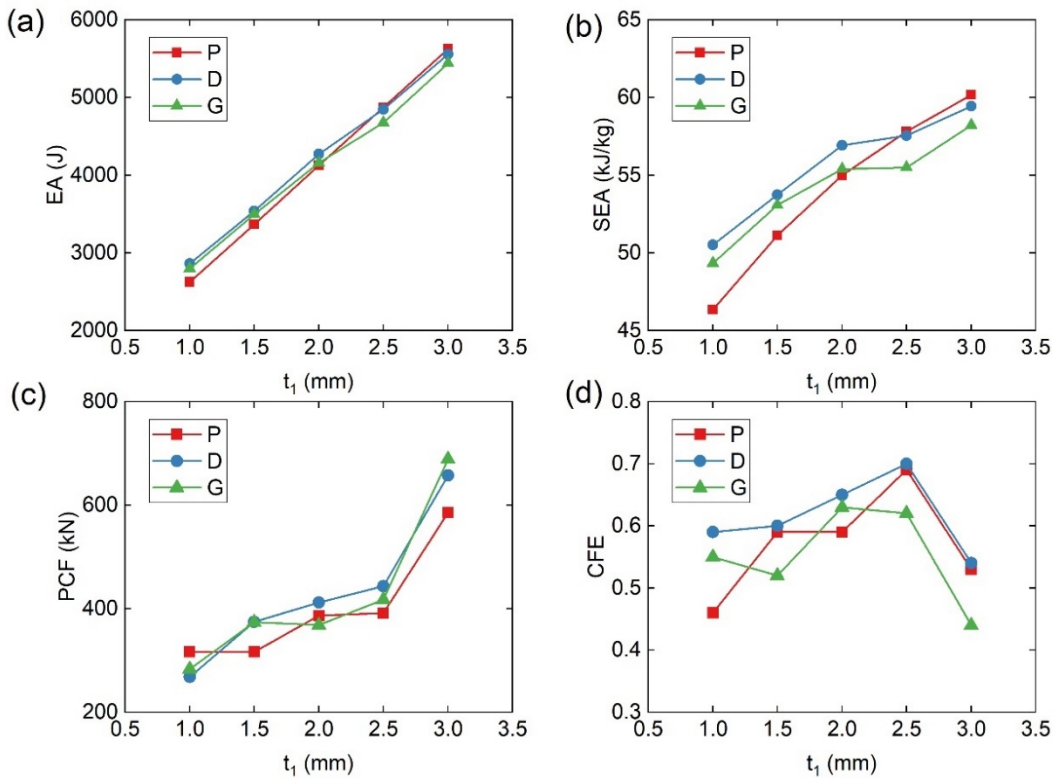


**Figure 7.** Comparison of (a) EA, (b) SEA, (c) PCF, and (d) CFE with different  $t_1$ .

Table 4 and Figure 7 give the calculated results of structural crashworthiness indicators. It is shown that the EA and SEA of all three TPMS-CS structures increase with the increase of  $t_1$ , and the P-TPMS-CS with  $t_1 = 3$  mm has the highest EA (5623.44 J) and SEA (60.16 kJ/kg). The results indicate that the P-TPMS-CS and D-TPMS-CS exhibit better energy absorption ability.

The PCF of all the TPMS-CS structures also increases with the increase of  $t_1$  and increases rapidly while the  $t_1$  is bigger than 2.5 mm. The G-TPMS-CS has the highest PCF (688.81 kN) at  $t_1 = 3$  mm.

For the crushing force efficiency, the CFE of P, D-TPMS-CS structures first increase with the increase of  $t_1$  and then decreases with the increase of  $t_1$  at  $t_1 = 2.5$  mm. There is no obvious trend in the CFE of G-TPMS-CS structures. The D-TPMS-CS have the highest CFE (0.7) at  $t_1 = 2.5$  mm.

### 3.2.2. The influence of $t_2$

To investigate the effect of the outer shell thickness  $t_2$  on the crashworthiness of TPMS-CS, the FE analysis was carried out by changing the  $t_2$  from 1 mm to 3 mm. All the TPMS-CS structures have identical parameters for inner shell thickness  $t_1 = 2$  mm and  $RD = 20\%$ .

Figure 8 plots the force-displacement curves of three TPMS-CS structures with different  $t_2$ . All the force-displacement curves have similar trends. It can be seen that all the crushing force responses are increased with the increase of  $t_2$ .

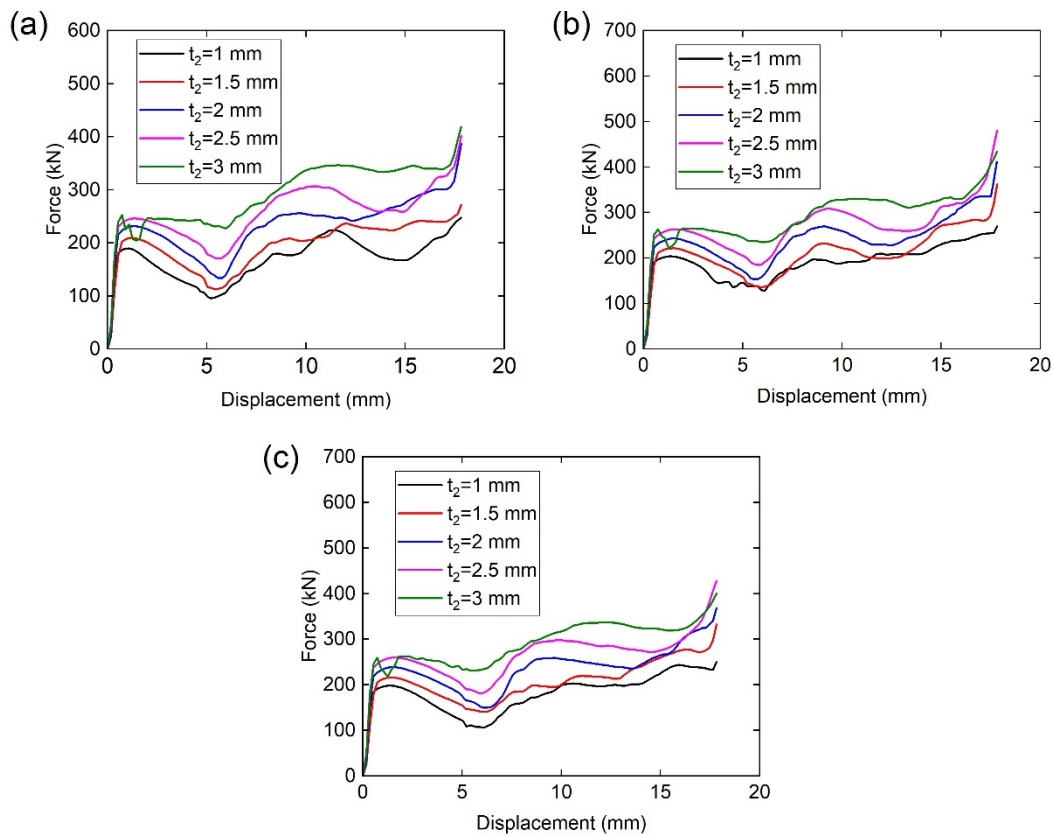


**Figure 8.** Force–displacement curves of (a) P-TPMS-CSs, (b) D-TPMS-CSs, and (c) G-TPMS-CSs for different  $t_2$ .

**Table 5.** Influence of  $t_2$  on crashworthiness indicators of TPMS-CS structures.

TPMS	$t_2$ (mm)	EA (J)	PCF (kN)	SEA (kJ/kg)	CFE
P	1	3010.19	247.62	46.60	0.68
	1.5	3473.58	272.14	49.74	0.66
	2	4126.79	386.62	54.98	0.59
	2.5	4562.29	401.88	56.82	0.63
	3	5180.25	418.58	60.57	0.64
D	1	3402.73	269.93	52.67	0.7
	1.5	3740.50	362.63	53.57	0.67
	2	4272.38	412	56.92	0.62
	2.5	4780.99	420.25	59.55	0.64
	3	5192.63	410.63	60.72	0.66
G	1	3228.56	250.35	49.98	0.72
	1.5	3669.70	332.73	52.55	0.61
	2	4158.38	368.61	55.40	0.63
	2.5	4681.38	428.02	58.30	0.61
	3	5128.39	400.52	59.96	0.63

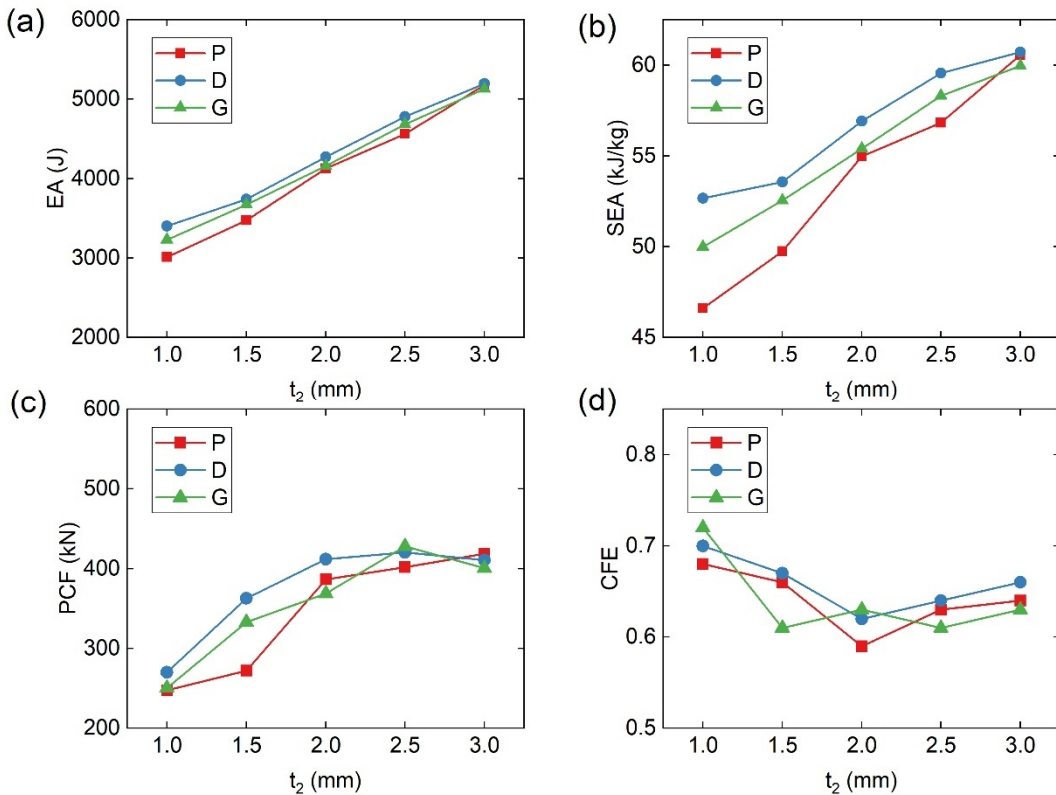


**Figure 9.** Comparison of (a) EA, (b) SEA, (c) PCF, and (d) CFE with different  $t_2$ .

Table 5 and Figure 9 give the calculated results of structural crashworthiness indicators. It is shown that the EA and SEA of all three TPMS-CS structures increased with the increase of  $t_1$ , and the D-TPMS-CS with  $t_2 = 3$  mm has the highest EA (5192.63 J) and SEA (60.72 kJ/kg). The results indicate that the D-TPMS-CS exhibits better energy absorption ability.

The PCF of all the TPMS-CS structures also increases with the increase of  $t_2$ , and the PCF increases slowly at high outer shell thickness. The P-TPMS-CS have the highest PCF (418.58 kN) at  $t_2 = 3$  mm.

For the crushing force efficiency, the CFE of all the TPMS-CS structures first decreases with the increase of  $t_2$  and then increases past  $t_2 = 2$  mm. The G-TPMS-CS have the highest CFE (0.72) at  $t_2 = 1$  mm.

### 3.2.3. The influence of RD

To investigate the influence of the TPMS filled relative density  $RD$  on the crashworthiness of TPMS-CS, the FE analysis was carried out by changing the  $RD$  from 10% to 30%. All the TPMS-CS structures have identical parameters for outer shell thickness  $t_2 = 2$  mm and inner shell thickness  $t_1 = 2$  mm.

Figure 10 plots the force-displacement curves of three TPMS-CS structures with different  $RD$ . All the force-displacement curves have similar trends. It can be seen that all the crushing force responses are increased with the increase of  $RD$ .

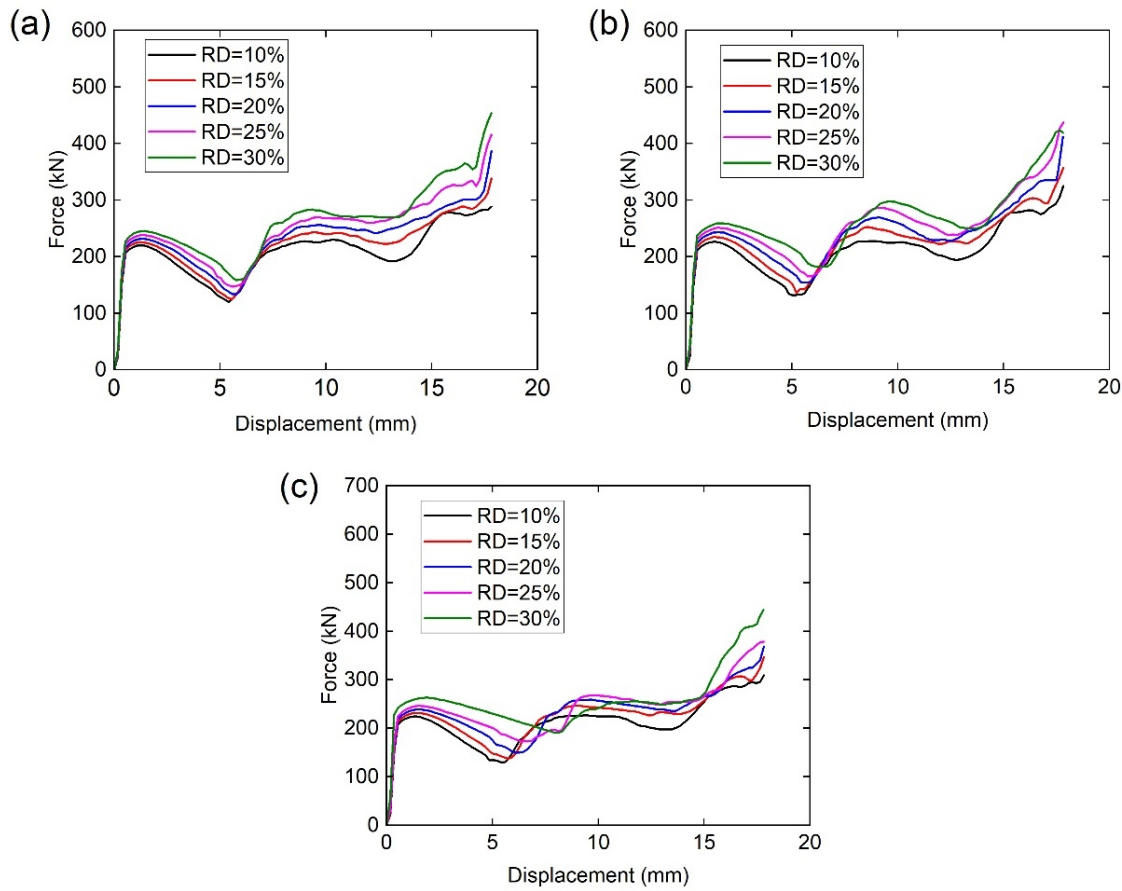


**Figure 10.** Force–displacement curves of (a) P-TPMS-CSs, (b) D-TPMS-CSs, and (c) G-TPMS-CSs for different  $RD$ .

**Table 6.** Influence of  $RD$  on crashworthiness indicators of TPMS-CS structures.

TPMS	$RD$ (%)	EA (J)	PCF (kN)	SEA (kJ/kg)	CFE
P	10	3692.58	287.98	55.61	0.66
	15	3916.53	338.1	55.37	0.64
	20	4126.79	386.62	54.98	0.59
	25	4400.68	415.63	55.42	0.59
	30	4653.71	454.06	55.59	0.57
D	10	3765.75	325.32	56.71	0.64
	15	4048.45	357.1	57.23	0.63
	20	4272.38	372.24	56.92	0.64
	25	4538.83	386.46	57.16	0.65
	30	4707.5	423.33	56.22	0.62
G	10	3753.15	309.67	56.52	0.67
	15	4004.82	347.01	56.62	0.64
	20	4158.38	368.61	55.40	0.63
	25	4311.71	378.74	54.31	0.63
	30	4560.05	444	54.47	0.57

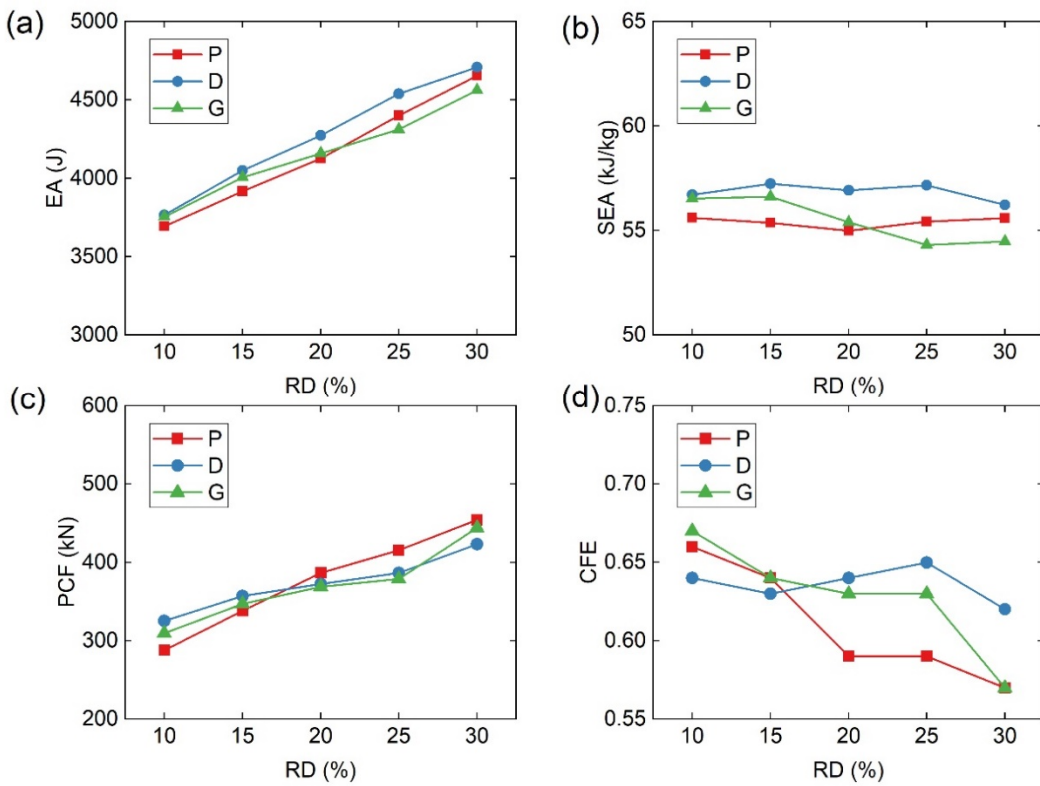


**Figure 11.** Comparison of (a) EA, (b) SEA, (c) PCF, and (d) CFE with different *RD*.

Table 6 and Figure 11 give the calculated results of structural crashworthiness indicators. It is shown that the EA of all three TPMS-CS structures increased with the increase of *RD*, and the D-TPMS-CS with *RD* = 30% have the highest EA (4707.5 J). The EA of all the TPMS-CS structures is almost constant with the increase of *RD*.

The PCF of all the TPMS-CS structures also increases with the increase of *RD*. The P-TPMS-CS have the highest PCF (454.06 kN) at *RD* = 30%.

For the crushing force efficiency, the CFE of P, G-TPMS-CS structures decreases with the increase of *RD*. There is no obvious trend in the CFE of D-TPMS-CS structures. The results indicate that the *RD* of TPMS-CS structures should be properly adopted.

#### 4. Multi-objective crashworthiness optimization

##### 4.1. Optimization methodology

###### 4.1.1. Definition of the optimization problem

In crashworthiness applications, the TPMS-CS structures should absorb as much energy as possible, while the PCF should be limited within a threshold value to guarantee the security of occupants [31–33]. In this regard, the optimization objectives of the TPMS-CS are to maximum *SEA* and minimum *PCF*. From the previous section, the simulation results indicate that the diamond TPMS-CS structures exhibit superior crashworthiness performances. Thus, we conduct the optimization design for the diamond TPMS-CS structures in this section.

From the discussion in the previous section, the crashworthiness indicators of the TPMS-CSs are affected by the inner shell thickness ( $t_1$ ), outer shell thickness ( $t_2$ ), and the relative density of TPMS ( $RD$ ). Therefore, the mathematical optimization formulation for this optimization problem can be defined as follows,

$$\begin{cases} \text{Min.} & \{-SEA(t_1, t_2, RD), PCF(t_1, t_2, RD)\} \\ \text{s. t.} & 1\text{mm} \leq t_1, t_2 \leq 2\text{mm} \\ & 0.1 \leq RD \leq 0.3 \end{cases} \quad (6)$$

#### 4.1.2. Design of experiment (DOE)

To generate the surrogate models, the first step is to sample the reasonable design sampling points. Design of Experiment (DOE) is the typical way to address how to explore the entire design space properly. Among the available DOE techniques, the Latin Hypercube sampling (LHS) is adopted because it can efficiently produce the uniformly-distributed sampling points in the design space [34,35].

#### 4.1.3. Surrogate models and error metrics

Crashworthiness optimization typically needs a larger amount of simulations. As an effective alternative, surrogate models are usually employed in literature to calculate the values of the objective function. In this study, three kinds of surrogate models, namely, Kriging (KRG) [36], polynomial response surface (PRS) [37], and radial basis function (RBF) [38] are used to approximate the objective function responses. The core functions of these surrogate models are listed in Table 7.

**Table 7.** Core functions of three surrogate models [39].

Surrogate model	Approximate function $\hat{y}(\mathbf{x})$	Correlation function
KRG	$\hat{\beta} + \mathbf{r}^T(\mathbf{x})\mathbf{R}^{-1}(\mathbf{y} - \mathbf{f}\hat{\beta})$	$R(\mathbf{x}^i, \mathbf{x}^j) = \exp\left(-\sum_{k=1}^m \theta_k  x_k^i - x_k^j ^2\right)$ $0.05 \leq \theta_k \leq 100$
PRS	$b_0 + \sum_{i=1}^n b_i x_i + \sum_{i=1}^n \sum_{j=1}^n b_{ij} x_i x_j + \sum_{i=1}^n \sum_{j=1}^n \sum_{k=1}^n b_{ijk} x_i x_j x_k$	None
RBF	$\sum_{i=1}^{n_s} \lambda_i \varphi(r(\mathbf{x}_i, \mathbf{x}))$	$\varphi(r(\mathbf{x}_i, \mathbf{x})) = \sqrt{\ \mathbf{x} - \mathbf{x}_i\ ^2 + c^2}$ $c = 1.0$

To evaluate the accuracy of these three different surrogate models, additional assessment sample points should be generated. Three kinds of metrics, namely, square value ( $R^2$ ), relative average absolute error (RAAE), and relative maximum absolute error (RMAE) are used in this study [40, 41]. The mathematic expression of these metrics is given as,

$$R^2 = 1 - \frac{\sum_{i=1}^q (y_i - \hat{y}_i)^2}{\sum_{i=1}^q (y_i - \bar{y})^2} \quad (7)$$

$$RAAE = \frac{\sum_{i=1}^q |y_i - \hat{y}_i|}{\sum_{i=1}^q |y_i - \bar{y}|} \quad (8)$$

$$RMAE = \frac{\max\{|\hat{y}_1 - y_1|, \dots, |\hat{y}_q - y_q|\}}{\sum_{i=1}^q |y_i - \bar{y}|/q} \quad (9)$$

where  $y_i$  is the exact function value at the assessment point  $i$ ,  $\hat{y}$  is the corresponding surrogate value,  $\bar{y}$  is the mean value of  $y_i$ , and  $q$  is the number of assessment points.

In general, the  $R^2$  and RAAE indicates the overall performance of the surrogate model, while the RMAE indicates the local accuracy of the surrogate model. Overall, the larger the  $R^2$ , or the smaller the RMSE and RMAE, the better the accuracy of the surrogate model.

#### 4.1.3. The procedure of the optimization design

To solve the proposed optimization problem, a multi-objective optimization method using the surrogate models and the multi-objective particle swarm optimization (MOPSO) algorithm [42,43] was developed. Firstly, the design points were generated using the Latin hypercube sampling (LHS) method. Secondly, the objective responses for the TPMS-CS structures were derived using the FE model at the design points. Three different kinds of surrogate models were constructed, and the error metrics were compared to choose the most accurate one for the following optimization design. Finally, the MOPSO algorithm was used to obtain the Pareto optimal solutions.

### 4.2. Optimization results and discussions

#### 4.2.1. Accuracy evaluation of the surrogate models

In this study, 40 training points were selected from the design space by the LHS method to construct the surrogate models. To evaluate the accuracy of the surrogate models, additional 10 assessment sampling points were generated from the design space and the error metrics of three surrogate models are listed in Table 8. It is shown that the KRG surrogate model exhibits the best accuracy performance. Thus, the KRG model was used to evaluate the objective value of the D-TPMS-CS structures in the following optimization design.

**Table 8.** Error metrics of the three surrogate models.

Surrogate model	Response	$R^2$	RAAE	RMAE
KGR	SEA	0.9750	0.1251	0.2954
	PCF	0.9351	0.1691	0.4205
PRS	SEA	0.9708	0.1454	0.3295
	PCF	0.8667	0.3211	0.4905
RBF	SEA	0.9334	0.2160	0.4070
	PCF	0.7429	0.2911	0.5734

#### 4.2.2. Multi-objective optimization results and discussions

The Pareto frontier of the D-TPMS-CS structure for the optimization problem was plotted in Figure 12. To guarantee the safety of the occupants, the PCF value was limited to 300 kN in this study, and the optimum design ( $t_1 = 1$  mm,  $t_2 = 2.87$  mm, and  $RD = 17.6\%$ ) was selected from the Pareto frontier. Furthermore, the FE analysis was carried out on the optimum points to obtain the FE values which were compared with the optimization results, as listed in Table 9. It can be found that the error between the surrogate model predicted value and FE simulation value in the PCF and SEA is less than 7%, which indicates the proposed optimization framework has high accuracy and acceptability.

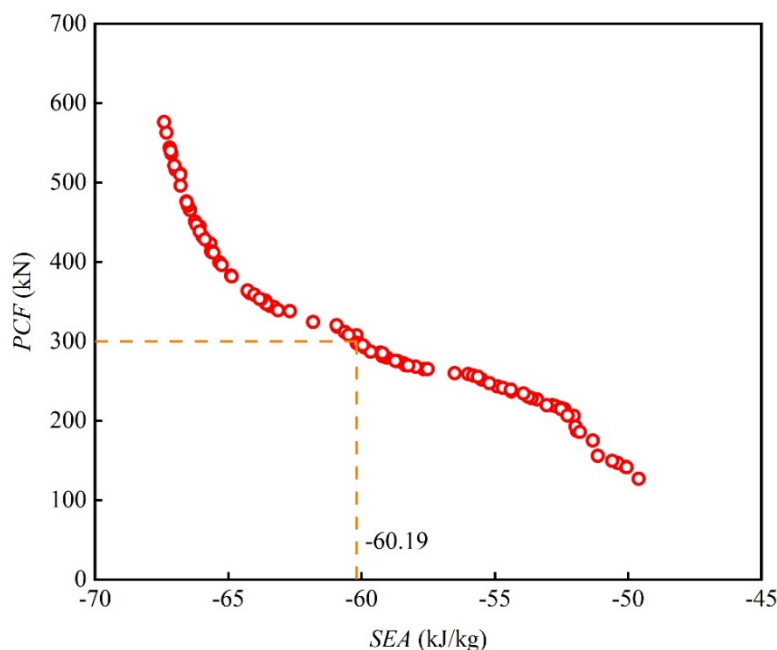


**Figure 12.** Pareto frontier for the D-TPMS-CS structure.

**Table 9.** Comparison between predicted value and FE value.

Indicator	FE value	Predict value	Error (%)
SEA (kJ/kg)	57.17	60.19	5.28
PCF (kN)	319.56	298.08	-6.72

## 5. Conclusions

In this paper, a series of novel TPMS lattices filled cylindrical shell (TPMS-CS) structures are proposed and their energy absorption properties are studied using FE analysis. The comparison of crashworthiness among different TPMS-CS structures, the parametric studies, and the multi-objective optimization design is conducted in this study. Some conclusions can be concluded as follows:

- By analyzing the energy absorption performances of three different TPMS-CS structures under axial loading, the SEA of D-TPMS-CS increased by 2.7% and 3.5% than the other two TPMS-CS structures. It can be concluded that the D-TPMS-CS structure exhibits the highest energy absorption ability and efficiency than the other two structures.

- The parametric studies show that the inner shell thickness, outer shell thickness, and relative density of filled TPMS have significant influence on the crashworthiness performances of TPMS-CS structures.
- The multi-objective optimization design method, which combines three surrogate models (KRG, PRS, RBF) and a multi-objective particle swarm optimization algorithm, was carried out to seek the optimum configuration of D-TPMS-CS structure ( $t_1 = 1$  mm,  $t_2 = 2.87$  mm, and  $RD = 17.6\%$ ). The relative errors of the proposed method are less than 7%.

## Acknowledgments

This work was supported by the Science and Technology Research Project of Education Department of Hubei Province (Grant No. B2022006), the WUST national defence preresearch foundation (Grant No. GF202010). Numerical calculation is supported by High-Performance Computing Center of Wuhan University of Science and Technology.

## Conflict of interest

The authors declare there is no conflict of interest.

## References

1. T. N. Doan, N. T. Thanh, P. Van Chuong, N. C. Tho, N. T. Ta, H. N. Nguyen, Analysis of stress concentration phenomenon of cylinder laminated shells using higher-order shear deformation Quasi-3D theory, *Compos. Struct.*, **232** (2020), 111526. <https://doi.org/10.1016/j.compstruct.2019.111526>
2. P. Jiao, Z. Chen, H. Ma, P. Ge, Y. Gu, H. Miao, Buckling behaviors of thin-walled cylindrical shells under localized axial compression loads, Part 1: Experimental study, *Thin-Walled Struct.*, **166** (2021), 108118. <https://doi.org/10.1016/J.Tws.2021.108118>
3. H. Wagner, C. Hühne, M. Janssen, Buckling of cylindrical shells under axial compression with loading imperfections: An experimental and numerical campaign on low knockdown factors, *Thin-Walled Struct.*, **151** (2020), 106764. <https://doi.org/10.1016/J.Tws.2020.106764>
4. S. M. Hosseini, M. Shariati, Experimental analysis of energy absorption capability of thin-walled composite cylindrical shells by quasi-static axial crushing test, *Thin-Walled Struct.*, **125** (2018), 259–268. <https://doi.org/10.1016/j.tws.2018.01.026>
5. D. Karagiozova, N. Jones, Dynamic effects on buckling and energy absorption of cylindrical shells under axial impact, *Thin-Walled Struct.*, **39** (2001), 583–610. [https://doi.org/10.1016/S0263-8231\(01\)00015-5](https://doi.org/10.1016/S0263-8231(01)00015-5)
6. P. B. Su, B. Han, M. Yang, Z. H. Wei, Z. Y. Zhao, Q. C. Zhang, et al., Axial compressive collapse of ultralight corrugated sandwich cylindrical shells, *Mater. Des.*, **160** (2018), 325–337. <https://doi.org/10.1016/j.matdes.2018.09.034>
7. H. Zhu, P. Wang, D. Wei, J. Si, Y. Wu, Energy absorption of diamond lattice cylindrical shells under axial compression loading, *Thin-Walled Struct.*, **181** (2022), 110131. <https://doi.org/10.1016/j.tws.2022.110131>

8. Y. Wang, X. Ren, Z. Chen, Y. Jiang, X. Cao, S. Fang, et al., Numerical and experimental studies on compressive behavior of Gyroid lattice cylindrical shells, *Mater. Des.*, **186** (2020), 108340. <https://doi.org/10.1016/j.matdes.2019.108340>
9. H. Huang, Q. Han, Nonlinear elastic buckling and postbuckling of axially compressed functionally graded cylindrical shells, *Int. J. Mech. Sci.*, **51** (2009), 500–507. <https://doi.org/10.1016/j.ijmecsci.2009.05.002>
10. Y. Wu, L. Sun, P. Yang, J. Fang, W. Li, Energy absorption of additively manufactured functionally bi-graded thickness honeycombs subjected to axial loads, *Thin-Walled Struct.*, **164** (2021), 107810. <https://doi.org/10.1016/j.tws.2021.107810>
11. J. Fang, G. Sun, N. Qiu, T. Pang, S. Li, Q. Li, On hierarchical honeycombs under out-of-plane crushing, *Int. J. Solids Struct.*, **135** (2018), 1–13. <https://doi.org/10.1016/j.ijsolstr.2017.08.013>
12. X. Niu, F. Xu, Z. Zou, T. Fang, S. Zhang, Q. Xie, In-plane dynamic crashing behavior and energy absorption of novel bionic honeycomb structures, *Compos. Struct.*, **299** (2022), 116064. <https://doi.org/10.1016/j.compstruct.2022.116064>
13. X. Niu, F. Xu, Z. Zou, Bionic inspired honeycomb structures and multi-objective optimization for variable graded layers, *J. Sandwich Struct. Mater.*, **25** (2023), 215–231. <https://doi.org/10.1177/10996362221127969>
14. M. F. Ashby, The properties of foams and lattices, *Phil. Trans. R. Soc. A*, **364** (2006), 15–30. <https://doi.org/10.1098/rsta.2005.1678>
15. H. S. Abdulhadi, A. Mian, Effect of strut length and orientation on elastic mechanical response of modified body-centered cubic lattice structures, *Proc. Inst. Mech. Eng., Part L: J. Mater.: Des. Appl.*, **233** (2019), 2219–2233. <https://doi.org/10.1177/1464420719841084>
16. Y. Wang, B. Ramirez, K. Carpenter, C. Naify, D. C. Hofmann, C. Daraio, Architected lattices with adaptive energy absorption, *Extreme Mech. Lett.*, **33** (2019), 100557. <https://doi.org/10.1016/J.Eml.2019.100557>
17. Y. Zhang, Z. Xue, L. Chen, D. Fang, Deformation and failure mechanisms of lattice cylindrical shells under axial loading, *Int. J. Mech. Sci.*, **51** (2009), 213–221. <https://doi.org/10.1016/j.ijmecsci.2009.01.006>
18. L. Chen, J. Zhang, B. Du, H. Zhou, H. Liu, Y. Guo, et al., Dynamic crushing behavior and energy absorption of graded lattice cylindrical structure under axial impact load, *Thin-Walled Struct.*, **127** (2018), 333–343. <https://doi.org/10.1016/j.tws.2017.10.048>
19. B. Du, L. Chen, W. Wu, H. Liu, Y. Zhao, S. Peng, et al., A novel hierarchical thermoplastic composite honeycomb cylindrical structure: Fabrication and axial compressive properties, *Compos. Sci. Technol.*, **164** (2018), 136–145. <https://doi.org/10.1016/j.compscitech.2018.05.021>
20. Y. Wu, J. Fang, C. Wu, C. Li, G. Sun, Q. Li, Additively manufactured materials and structures: A state-of-the-art review on their mechanical characteristics and energy absorption, *Int. J. Mech. Sci.*, **246** (2023), 108102. <https://doi.org/10.1016/j.ijmecsci.2023.108102>
21. N. Qiu, J. Zhang, F. Yuan, Z. Jin, Y. Zhang, J. Fang, Mechanical performance of triply periodic minimal surface structures with a novel hybrid gradient fabricated by selective laser melting, *Eng. Struct.*, **263** (2022), 114377. <https://doi.org/10.1016/j.engstruct.2022.114377>
22. L. Zhang, S. Feih, S. Daynes, S. Chang, M. Y. Wang, J. Wei, et al., Energy absorption characteristics of metallic triply periodic minimal surface sheet structures under compressive loading, *Addit. Manuf.*, **23** (2018), 505–515. <https://doi.org/10.1016/j.addma.2018.08.007>

23. N. Qiu, J. Zhang, C. Li, Y. Shen, J. Fang, Mechanical properties of three-dimensional functionally graded TPMS structures, *Int. J. Mech. Sci.*, **246** (2023), 108118. <https://doi.org/10.1016/j.ijmecsci.2023.108118>

24. H. Yin, Z. Liu, J. Dai, G. Wen, C. Zhang, Crushing behavior and optimization of sheet-based 3D periodic cellular structures, *Composites, Part B*, **182** (2020), 107565. <https://doi.org/10.1016/j.compositesb.2019.107565>

25. O. Al-Ketan, R. K. Abu Al-Rub, Multifunctional mechanical metamaterials based on triply periodic minimal surface lattices, *Adv. Eng. Mater.*, **21** (2019), 1900524. <https://doi.org/10.1002/Adem.201900524>

26. H. Sun, C. Ge, Q. Gao, N. Qiu, L. Wang, Crashworthiness of sandwich cylinder filled with double-arrowed auxetic structures under axial impact loading, *Int. J. Crashworthiness*, **27** (2022), 1383–1392. <https://doi.org/10.1080/13588265.2021.1947071>

27. Y. Wu, J. Fang, Y. He, W. Li, Crashworthiness of hierarchical circular-joint quadrangular honeycombs, *Thin-Walled Struct.*, **133** (2018), 180–191. <https://doi.org/10.1016/j.tws.2018.09.044>

28. Y. Wu, J. Fang, Z. Cheng, Y. He, W. Li, Crashworthiness of tailored-property multi-cell tubular structures under axial crushing and lateral bending, *Thin-Walled Struct.*, **149** (2020), 106640. <https://doi.org/10.1016/j.tws.2020.106640>

29. Y. Zhang, M. Lu, C. H. Wang, G. Sun, G. Li, Out-of-plane crashworthiness of bio-inspired self-similar regular hierarchical honeycombs, *Compos. Struct.*, **144** (2016), 1–13. <https://doi.org/10.1016/j.compstruct.2016.02.014>

30. G. Sun, S. Li, Q. Liu, G. Li, Q. Li, Experimental study on crashworthiness of empty/aluminum foam/honeycomb-filled CFRP tubes, *Compos. Struct.*, **152** (2016), 969–993. <https://doi.org/10.1016/j.compstruct.2016.06.019>

31. J. Fang, G. Sun, N. Qiu, N. H. Kim, Q. Li, On design optimization for structural crashworthiness and its state of the art, *Struct. Multidiscip. Optim.*, **55** (2017), 1091–1119. <https://doi.org/10.1007/s00158-016-1579-y>

32. J. Fang, Y. Gao, G. Sun, G. Zheng, Q. Li, Dynamic crashing behavior of new extrudable multi-cell tubes with a functionally graded thickness, *Int. J. Mech. Sci.*, **103** (2015), 63–73. <https://doi.org/10.1016/j.ijmecsci.2015.08.029>

33. G. Sun, T. Pang, J. Fang, G. Li, Q. Li, Parameterization of criss-cross configurations for multiobjective crashworthiness optimization, *Int. J. Mech. Sci.*, **124** (2017), 145–157. <https://doi.org/10.1016/j.ijmecsci.2017.02.027>

34. J. S. Park, Optimal Latin-hypercube designs for computer experiments, *J. Stat. Plann. Inference*, **39** (1994), 95–111. [https://doi.org/10.1016/0378-3758\(94\)90115-5](https://doi.org/10.1016/0378-3758(94)90115-5)

35. N. Qiu, Y. Gao, J. Fang, Z. Feng, G. Sun, Q. Li, Crashworthiness analysis and design of multi-cell hexagonal columns under multiple loading cases, *Finite Elem. Anal. Des.*, **104** (2015), 89–101. <https://doi.org/10.1016/j.finel.2015.06.004>

36. Y. Wu, W. Li, J. Fang, Q. Lan, Multi-objective robust design optimization of fatigue life for a welded box girder, *Eng. Optim.*, **50** (2018), 1252–1269. <https://doi.org/10.1080/0305215X.2017.1395023>

37. X. Song, G. Sun, G. Li, W. Gao, Q. Li, Crashworthiness optimization of foam-filled tapered thin-walled structure using multiple surrogate models, *Struct. Multidiscip. Optim.*, **47** (2013), 221–231. <https://doi.org/10.1007/s00158-012-0820-6>

38. H. M. Gutmann, A radial basis function method for global optimization, *J. Global Optim.*, **19** (2001), 201–227. <https://doi.org/10.1023/A:1011255519438>
39. A. I. J. Forrester, A. J. Keane, Recent advances in surrogate-based optimization, *Prog. Aerosp. Sci.*, **45** (2009), 50–79. <https://doi.org/10.1016/j.paerosci.2008.11.001>
40. J. Fu, Q. Liu, K. Liufu, Y. Deng, J. Fang, Q. Li, Design of bionic-bamboo thin-walled structures for energy absorption, *Thin-Walled Struct.*, **135** (2019), 400–413. <https://doi.org/10.1016/j.tws.2018.10.003>
41. N. Qiu, Z. Jin, J. Liu, L. Fu, Z. Chen, N. H. Kim, Hybrid multi-objective robust design optimization of a truck cab considering fatigue life, *Thin-Walled Struct.*, **162** (2021), 107545. <https://doi.org/10.1016/j.tws.2021.107545>
42. C. A. C. Coello, G. T. Pulido, M. S. Lechuga, Handling multiple objectives with particle swarm optimization, *IEEE Trans. Evol. Comput.*, **8** (2004), 256–279. <https://doi.org/10.1109/TEVC.2004.826067>
43. J. Fang, Y. Gao, G. Sun, N. Qiu, Q. Li, On design of multi-cell tubes under axial and oblique impact loads, *Thin-Walled Struct.*, **95** (2015), 115–126. <https://doi.org/10.1016/j.tws.2015.07.002>



AIMS Press

©2023 the Author(s), licensee AIMS Press. This is an open access article distributed under the terms of the Creative Commons Attribution License (<http://creativecommons.org/licenses/by/4.0>)